Journal of Colloid and Interface Science 604 (2021) 550–561

Contents lists available at ScienceDirect

Journal of Colloid and Interface Science

journal homepage: www.elsevier.com/locate/jcis

Evaporation-triggered directional transport of asymmetrically confined droplets

Xukun He [a], Jiangtao Cheng [a,b,c,*]

[a] Department of Mechanical Engineering, Virginia Tech, Blacksburg, VA 24061, USA
[b] Macromolecules Innovation Institute, Virginia Tech, Blacksburg, VA 24061, USA
[c] Center for Soft Matter and Biological Physics, Virginia Tech, Blacksburg, VA 24061, USA

GRAPHICAL ABSTRACT

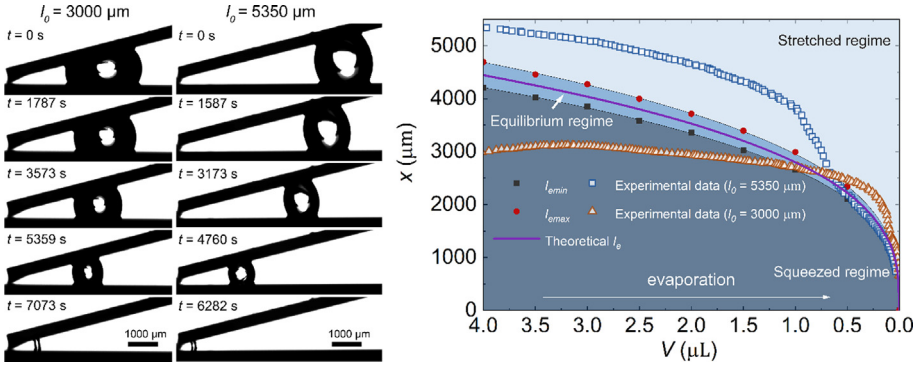

ARTICLE INFO

Article history:
Received 19 April 2021
Revised 27 June 2021
Accepted 28 June 2021
Available online 5 July 2021

Keywords:
Droplet evaporation
Evaporation-triggered droplet actuation
Self-relaxation process
Stretched/squeezed droplet state
Unidirectional transport
Asymmetric confinement

ABSTRACT

Hypothesis: When a liquid droplet is confined between two non-parallel hydrophobic surfaces with dihedral angle α, its behavior is largely influenced by the asymmetric confinement. During evaporation, the droplet morphology under confinement will continuously evolve, leading to the directional transport of the droplet towards the cusp.

Experiments and Simulations: During the evaporation process, droplets at different initial locations l_0 from the cusp were experimentally observed to transport towards the cusp. A series of simulations using Surface Evolver were performed to obtain the three-dimensional morphologies of the confined droplets. Force and energy analyses were conducted to unveil the mechanisms dominating the evaporation-triggered actuation and transport.

Findings: The asymmetrically confined droplet of volume V would drift towards an equilibrium location of l_e from the cusp with the lowest energy. Its directional motion results from the consecutively decreasing l_e, which is scaled as $l_e \sim \alpha^{-1}V^{\frac{1}{3}}$ during evaporation. Herein, the creeping and slipping modes of transport could be characterized as the quasi-stable and unstable self-relaxation processes of droplet from the stretched regime to the equilibrium regime, respectively. Our findings on the intrinsic mechanism of droplet actuation shed light on a novel approach to manipulating the confined droplet behaviors in a passive and decisive fashion.

* Corresponding author at Department of Mechanical Engineering, Virginia Tech, Blacksburg, VA 24061, USA.
E-mail address: chengjt@vt.edu (J. Cheng).

https://doi.org/10.1016/j.jcis.2021.06.164
0021-9797/

1. Introduction

Evaporation of a sessile liquid droplet can lead to the enrichment and settlement of the contained analytes or colloidal particles after its complete evaporation, which has become an essential procedure in various applications including biosensing [1], bio/chemical analyses in droplet-based microfluidic systems [2,3] and nanomaterial syntheses [4,5]. As such, evaporation is one of the critical techniques to extract solutes or to achieve the self-assembly of colloidal particles for the syntheses of nanodevices [6,7]. When combined with sensing techniques such as surface-enhanced Raman spectroscopy (SERS) [8,9] and matrix-assisted laser desorption/ionization mass spectrometry (MALDI-MS) [10], the well-controlled droplet evaporation could be applied to concentrate the analytes on the sensing spot for the detection and identification of the targeted analytes/molecules with ultralow concentrations [8].

Correspondingly, the prescribed transport of the sample droplet towards the specific sensing spot before its complete evaporation is the prerequisite for the accurate screening of targeted analytes. During the past two decades, especially inspired by droplet motion on spider silk [11], cactus spines [12], and Cotula fallax plant [13], the directional transport of droplet has been realized through various strategies: (1) wettability gradient induced by surface textures [14], chemical functionalizations [15], thermal gradient [16] or electrowetting effect [17,18]; (2) external body forces including gravity [19], magnetic force [20] and electric force [21]; and (3) Laplace pressure difference due to the confinement in asymmetric geometries [11,22–28]. However, the complex geometric structures, extra force/temperature/concentration fields, and functionalized surfaces with fragile micro/nanostructures involved in these technologies still restrict their practical applications. Therefore, a passive method for the prescribed droplet transport on a simple platform or gadget is still highly desired.

Recently, a capillary ratchet mimicking the shorebird beak with two non-parallel hydrophilic surfaces, *i.e.*, wedge-shaped or V-shaped structure, has been applied to directionally transport the liquid bridge by periodically open-close the beak-like structure [26]. Even though still hampered by the complex mechanical operations, this simple V-shaped platform with asymmetric geometry does inspire us to achieve the directional transport of liquid droplets in a passive manner, which is incurred by the continuously evolving and asymmetric morphology of the droplet confined between two non-parallel surfaces during evaporation. As such, the evaporation of colloidal liquid bridges formed between two non-parallel hydrophilic surfaces and their special drying patterns have been reported [29,30]. However, in these studies, it was hard for the liquid bridges to get stabilized at a specific location because of the dominant effect of Laplace pressure [25,31]. As a result, the liquid bridge quickly moved towards and filled the corner of the V-shaped groove and the deposition pattern of solute/colloidal particles was not concentrated within a relatively small footprint due to the coffee-ring effect [29,32,33]. Thus, in this work, we consider using the lower-energy surfaces, *i.e.*, hydrophobic surfaces, to achieve the controllable transport of droplets in a passive manner while suppressing the coffee-ring effect. Different from the previous works which simply ascribe the asymmetric evaporation to the capillary force [27,34] without insightful analyses, here we would comprehensively investigate the effects of V-shaped geometry on both the evaporation and transport of a liquid droplet confined therein.

Through a series of experimental measurements, numerical simulation, and theoretical analysis, this work aims to explore the dynamic motion of an evaporating droplet confined between two non-parallel hydrophobic surfaces with dihedral angle α by addressing the following questions: (1) How does the asymmetrically confined droplet behave between two non-parallel hydrophobic surfaces during evaporation? (2) How is the confined droplet motion affected by droplet volume, droplet location and dihedral angle? And (3) what are the underlying mechanisms of this evaporation-triggered directional transport of the confined droplet? By conducting a comprehensive force and energy analysis on the confined droplet, we would address these questions to deepen our understanding of evaporating droplet dynamics in a confined space. In addition, the Surface Evolver simulation was conducted to obtain the three-dimensional (3D) morphology of the asymmetrically confined droplet and to validate our theoretical analyses in the context of our experimental observations. This previously unexplored study sheds light on a new approach to developing droplet-based microfluidic cargo system by taking advantage of asymmetric structures, in which the evaporation-triggered actuation of the confined droplet could be employed to achieve the simultaneous droplet directional transport and solute enrichment in otherwise inaccessible and extremely constrained region.

2. Experimental and simulation setup

2.1. Hydrophobic surfaces preparation and experimental setup

In this work, the hydrophobic plate surfaces were prepared by firstly cutting a silicon wafer into pieces with the dimension of 2 cm × 1 cm. Then the pieces of silicon wafer were primed by spin-coating with fluoropolymer (PFC 1601 V, Cytonix Corporation) at 3000 rpm for 30 s. After the samples being baked at 160 °C for 1 h, the static contact angle θ of water microdroplet on the samples could reach $118^\circ \pm 1^\circ$, while its advancing contact angle θ_a and receding contact angle θ_r were measured as $\sim 123^\circ$ and $\sim 107^\circ$, respectively. To study the transport of evaporating droplets confined between two non-parallel surfaces, one of the two identically prepared samples was first mounted onto a vertically adjustable linear-stage (stage #1, Metric Z-Axis Stage, Edmund Corporation). And the other sample was attached on the edge of a tiltable platform with a tilt-range of $-25^\circ \sim 25^\circ$ (stage #2, Ball and Socket Stage, M−RN−50, Newport Corporation). Then a deionized (DI) water droplet of 4 ± 0.1 μL (Type I, > 18 MΩ·cm resistivity) was deposited on the lower sample surface on stage #1, which was incrementally moved upwards till touching the upper sample surface on the stage #2. In this way, an initially stable droplet was confined between the two non-parallel surfaces. The configuration of our experimental setup is illustrated in Fig. 1a, in which the dihedral angle α and the initial position l_0 of the confined droplet were controlled by tilting the inclination of the upper platform and by adjusting the horizontal distance between the upper and lower surfaces. It has been demonstrated that an unstable liquid bridge would be automatically propelled towards the apex of two non-parallel hydrophilic surfaces within only a few seconds [24,25]. Therefore, after the droplet being sandwiched between the two non-parallel hydrophobic surfaces in our setup, we waited for at least 30 s to ensure that the confined droplet dwelling at a distance l_0 from the cusp was initially in a stable or quasi-stable state.

All the evaporation experiments were conducted in a custom-designed transparent chamber with the dimension of 20 cm × 20 cm × 20 cm, in which the relative humidity (RH) was controlled at 35–40% and the ambient temperature was maintained at 21 ± 1°C. An integrated camera on the contact angle measurement system (Theta Lite, OneAttension Corporation) was used to capture the transient images of the evaporating droplet at a rate

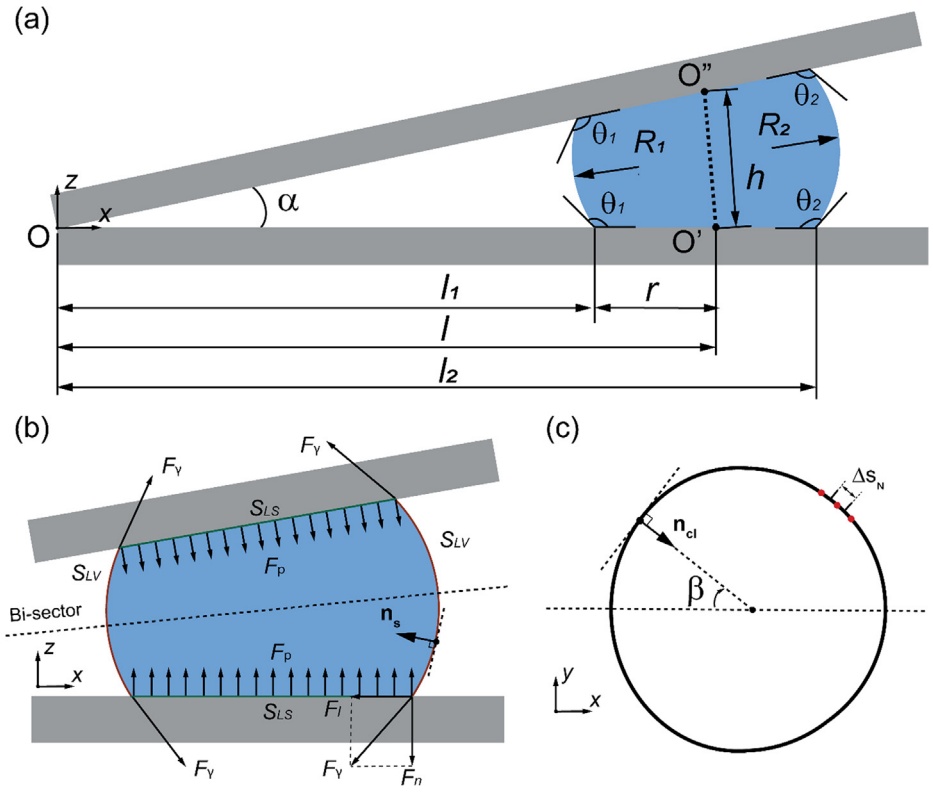

Fig. 1. (a) Schematic illustration of a droplet confined between two non-parallel hydrophobic surfaces, where O stands for the cusp or apex of the two non-parallel surfaces, h is the droplet height which is defined as the distance (O′O″) between the centers of its upper and lower contact areas. (b) Diagram of all forces exerted on the confined droplet. (c) Top view of the droplet contact base and contact line on the plate surface with in-plane coordinates (x, y). Here β is the azimuthal angle based on the centroid of the contact base and Δs_N is the length of contact line element connected to the Nth vertex in our simulation.

of 1.14 frames per second. The reproducibility of our experiments was verified by repeating each case at least three times.

2.2. Simulation setup

In our previous study [35], the evaporation of squeezed droplets between two parallel hydrophobic/superhydrophobic surfaces was found to be significantly suppressed due to the vapor enrichment inside the confined space. Thus, in this work, we assume the evaporation of confined droplets between two non-parallel surfaces as a quasi-steady process, which means the transient shape of an evaporating droplet could be approximated by its profile at the equilibrium state. Using the open-accessed software Surface Evolver [36], the profile of an evaporating droplet can be obtained by minimizing its surface energy under a set of constraints. In addition to the constraints of constant volume and static contact angle, we further implemented the algorithm developed by J.A. White [37,38] to account for the potential effect of contact angle hysteresis (CAH) on the contact line motion as following: (1) The dimensionless force $f_i = F_i/\gamma_{LV}\Delta l$ on certain vertex i along the solid–liquid–vapor triple-phase contact line is obtained from Surface Evolver by resorting a virtual displacement of the confined droplet, where F_i is the force on the vertex, γ_{LV} is the interfacial tension of liquid–vapor interface and Δl is the length of the two edges connected with the vertex; (2) The modulus of the dimensionless force f_i is compared with the maximum friction force f_{max}. If $f_i > f_{max}$, the vertex is allowed to move, otherwise the vertex is kept fixed. Here, the modulus of f_{max} is dependent on whether the vertex is advancing or receding:

$$f_{a\_max} = \cos\theta - \cos\theta_a \quad (1)$$

$$f_{r\_max} = \cos\theta_r - \cos\theta \quad (2)$$

where the advancing contact angle θ_a and the receding contact angle θ_r are chosen based on our experimental measurements during evaporation. The static contact angle θ is the averaged value of θ_a and θ_r. The detailed algorithm of this computational process is shown in the flowchart of Fig. S1 in the Supplementary Materials.

Besides, droplet volume V, dihedral angle α and distance l are three adjustable parameters in our Surface Evolver simulation that determine the equilibrium shape and position of the droplet. To eliminate the mesh-size effect, the number of the mesh grids N_{mesh} was initially set as 8200 to model the liquid–vapor interface of the droplet. During the simulation, the mesh was further optimized by implementing two internal functions, *i.e.*, "Equiangulation (u)" and "Vertex Averaging (V)", and a user-defined function that can refine or delete the excessively long or short edges. The predicted values of the contact radii of the confined droplet with varying α and l were found to be consistent with our experimental values as shown in Fig. S2, which could validate the methodology of our Surface Evolver simulation.

3. Theoretical analysis

3.1. The stability of confined droplet between two non-parallel surfaces

In general, the stability of a liquid bridge sandwiched between two non-parallel surfaces is determined by two necessary conditions [31,39]. First, the pressure inside the liquid droplet should be uniform so that the droplet can stay in equilibrium, thus the following geometrical relationship should be satisfied [23,31]:

$$\frac{\cos\left(\theta_2+\frac{\alpha}{2}\right)}{\cos\left(\theta_1-\frac{\alpha}{2}\right)}>1 \tag{3}$$

If the two surfaces are hydrophilic, θ_1 should be larger than $\theta_2+\alpha$, otherwise the instability induced by Laplace pressure difference inside the droplet could drive the droplet to move to the cusp. If the surfaces are hydrophobic, $\theta_1 < \theta_2+\alpha$ is required to reach droplet stability, which could be satisfied in all the three potential conditions of $\theta_1 < \theta_2$, $\theta_1 = \theta_2$, and $\theta_1 > \theta_2$, indicating that the dynamics, especially the moving direction, of the droplet confined between two non-parallel hydrophobic surfaces is indecisive. Even though this indecisive manner had been observed in previous work, no insightful explanation has been given [23]. Second, all the forces acting on the mass center of the droplet need to be balanced, entailing a comprehensive force analysis on the droplet between two non-parallel hydrophobic surfaces.

3.2. Force analysis of the confined droplet

First of all, the gravity effect on the dynamics of the evaporating microdroplet is neglected in this work due to the small Bond number ($\mathrm{Bo}=\rho g h^2/\gamma_{LV}\sim 0.1$, where ρ is water density and g is the gravity constant), which is evidenced by the almost identical contact radii of the confined droplet on both the upper and lower surfaces (Fig. S3). Thus, besides the surface tension force along the solid–liquid–vapor triple-phase contact line (*cl*), only the pressure-induced forces on the liquid–vapor interface S_{LV} and on the top and bottom liquid–solid interfaces $2S_{LS}$ are considered in our force analysis as shown in Fig. 1b.

The Laplace pressure-induced force $\boldsymbol{F_p}$ on the confined droplet could be calculated by integrating the pressure over the liquid–solid surface area $2S_{LS}$ and the liquid–vapor surface area S_{LV}:

$$\begin{aligned}\boldsymbol{F_p}&=\int_{S_{LV}} p_a\boldsymbol{n_s}\,dS+\int_{2S_{LS}}(p_a+p_\gamma)\,\boldsymbol{n_s}dS\\&=\int_{S_{LV}+2S_{LS}} p_a\boldsymbol{n_s}dS+\int_{2S_{LS}} p_\gamma\boldsymbol{n_s}dS\end{aligned} \tag{4}$$

where p_a is the atmospheric pressure which could be regarded as a constant in our analysis and $\boldsymbol{n}_s$ is the unit inward normal vector of the droplet surface. Based on the Young-Laplace equation, the Laplace pressure p_γ inside the droplet could be estimated as $p_\gamma\approx 2\gamma_{LV}H$, where the liquid–vapor interface tension $\gamma_{LV}=0.072$ N/m for water and H is the mean curvature of the liquid–vapor interface.

Based on Gauss's theorem, the first term on the right-hand side of Eq. (4) is zero as a result of the integration of a constant over an enclosure, thus the magnitude of $\boldsymbol{F_p}$ on one liquid–solid interface S_{LS} can be estimated as the pressure-induced force:

$$F_p=\int_{S_{LS}} 2\gamma_{LV}H\,dS\approx 2\pi r^2\gamma_{LV}H \tag{5}$$

where r is the contact radius on the plate surface. Note that the mean curvature H could be directly calculated by averaging the curvatures of the 3D equilibrium morphology of the droplet based on our Surface Evolver simulation. Besides, if only the 2D shapes of the confined droplet were collected from experiments, based on some approximations shown in Section S3, H could also be estimated as:

$$H\approx\frac{1}{2}\left(\frac{2\cos\theta}{h}+\frac{1}{r}\right) \tag{6}$$

where h is the height of the droplet as depicted in Fig. 1a. The surface tension force along the contact line $\boldsymbol{F}_\gamma$ could be decomposed into two components, *i.e.*, the lateral (in-plane) adhesion force $\boldsymbol{F_l}$ and the normal adhesion force $\boldsymbol{F_n}$. Here, the lateral adhesion force $\boldsymbol{F_l}$ on the contact line can be regarded as the friction force $\boldsymbol{F_f}$, and the magnitude of friction force $\boldsymbol{F_f}$ could be obtained as:

$$F_f=\int_{cl}\gamma_{LV}\cos\theta\cos\beta dl\approx\sum_{N=1}^{N_{max}=N_{cl}}\gamma_{LV}\cos\theta_N\cos\beta_N\Delta s_N \tag{7}$$

where β is the azimuthal angle along the contact line as shown in Fig. 1c. In our Surface Evolver simulation, F_f could be estimated in the discrete form, in which N_{cl} is the number of vertices on the contact line and Δs_N is the length of contact line element connected to the Nth vertex. θ_N and β_N are the local contact angle and the azimuthal angle of the Nth vertex, respectively. Here, the droplet contact area on the plate surfaces is approximated by a circular shape, which will be verified in Section 4.2. According to Eq. (7), the y component of $\gamma_{LV}\cos\theta$ of the friction force $\boldsymbol{F_f}$ on the top or bottom plate surface is cancelled. In 2D form, Eq. (7) could be approximated as $F_f\approx\pi\gamma_{LV}r(\cos\theta_a-\cos\theta_r)$, indicating that the asymmetric contact angle difference due to contact angle hysteresis ($\theta_a-\theta_r$) is the origin of the lateral adhesion force.

In the context of Surface Evolver, the magnitude of normal adhesion force $\boldsymbol{F_n}$ on the contact line can be obtained as:

$$F_n=\int_{cl}\gamma_{LV}\sin\theta\,dl\approx\sum_{N=1}^{N_{max}=N_{cl}}\gamma_{LV}\sin\theta_N\Delta s_N \tag{8}$$

To apply the global force balance, all the above-mentioned three forces on the top and bottom solid–liquid interfaces and on the triple-phase contact lines need to be projected onto the bisector (Fig. 1b) as:

$$\begin{aligned}&2\int_{S_{LS}}\underbrace{2\gamma_{LV}H\sin\frac{\alpha}{2}\boldsymbol{n_s}dS}_{\boldsymbol{F'_p}}+2\int\underbrace{\gamma_{LV}\cos\theta\cos\frac{\alpha}{2}\boldsymbol{n_{cl}}\,dl}_{\boldsymbol{F'_f}}-2\int_{cl}\\&\quad\underbrace{\gamma_{LV}\sin\theta\sin\frac{\alpha}{2}\boldsymbol{n_s}\,dl}_{\boldsymbol{F'_n}}\\&=\rho V\boldsymbol{a}\end{aligned} \tag{9}$$

where $\boldsymbol{F'_p}$, $\boldsymbol{F'_f}$ and $\boldsymbol{F'_n}$ are the projections of all the pressure-induced force $\boldsymbol{F_p}$, lateral adhesion force $\boldsymbol{F_f}$ and normal adhesion force $\boldsymbol{F_n}$ on the bisector, respectively. And the acceleration of the droplet $\boldsymbol{a}=0$ if all the forces are balanced.

Here, the direction of $\boldsymbol{F'_n}$ is dependent on the wettability of the surfaces, which always points to the cusp O between hydrophobic surfaces; the direction of $\boldsymbol{F'_p}$ is dependent on the mean curvature H, which always points away from the cusp O if the surfaces are hydrophobic; the direction of $\boldsymbol{F'_f}$ depends on the contact angle distribution along the contact line ($\cos\theta_1-\cos\theta_2$ in 2D), which was found to be determined by the resultant force of $\boldsymbol{F'_p}$ and $\boldsymbol{F'_n}$ based on our experimental and simulation results, which will be discussed in detail in Section 4.2.

3.3. Energy analysis of droplet behaviors in confined space

To further elucidate droplet behaviors between two non-parallel surfaces, we also conducted surface energy analysis on the confined droplet. The Gibbs free energy G for the confined droplet can be approximated as [40,41]:

$$G=\gamma_{LV}S_{LV}+(\gamma_{LS}-\gamma_{SV})S_{LS} \tag{10}$$

where γ_{LS} and γ_{SV} are the liquid–solid interfacial tension and the solid–vapor interfacial tension, respectively. Eq. (10) could be simplified by Young's equation $\gamma_{LS}-\gamma_{SV}=-\gamma_{LV}\cos\theta$ as:

$$G=\gamma_{LV}(S_{LV}-S_{LS}\cos\theta) \tag{11}$$

Based on our Surface Evolver simulation, the free energy G of the confined droplet with different volumes between the two non-parallel surfaces with varying dihedral angle α could be obtained. To incorporate the free energy evolution with the mass reduction during evaporation, the surface energy could be estimated in terms of droplet volume V, droplet location l, and dihedral angle α:

$$G = 2\gamma_{LV}\sqrt{\pi\alpha l V}\left(1 - \sqrt{\frac{V}{\pi^3\alpha^3 l^3}}\cos\theta\right) \tag{12}$$

where two approximations, *i.e.*, the droplet height could be approximated as $h \approx \alpha l$ and the droplet body could be approximated by the cylindrical shape, were taken in the derivation of Eq. (12), since the droplet contact angle $\theta \sim 110^\circ$ is not remarkably deviated from 90° and the dihedral angle is significantly smaller than the contact angle ($\alpha \ll \theta$) in our work. According to Eq. (12), the free energy G would decrease with decreasing droplet volume V during evaporation. Moreover, as the confined droplet moves towards the cusp with decreasing l, the trends of the two components $l^{\frac{1}{2}}$ and $l^{-\frac{3}{2}}$ in Eq. (12) are contrary, which might lead to an equilibrium location l_e with the lowest surface energy G_{min}.

For a droplet with a certain volume V confined between two non-parallel surfaces with fixed dihedral angle α, this equilibrium location l_e could be obtained by assuming the derivative of the free energy with respect to lateral displacement $dG/dl = 0$. So, we have

$$l_e = \frac{-2k_e\cos\theta}{\alpha}\left(\frac{V}{\pi}\right)^{\frac{1}{3}} \sim \alpha^{-1}V^{\frac{1}{3}} \tag{13}$$

where k_e is the correction factor of the two approximations we took above. According to Eq. (13), this equilibrium location would continuously shift towards the cusp, *i.e.*, $l_e \to 0$ as $V \to 0$, during the evaporation, manifesting the evaporation-triggered directional transport of an evaporating droplet.

4. Results and discussion

4.1. Evaporation-triggered lateral transport of droplets confined between two non-parallel hydrophobic surfaces

The behaviors of evaporating droplets with an initial volume of 4 μL, which were confined between two non-parallel hydrophobic surfaces with a fixed dihedral angle $\alpha = 14^\circ$ but at different initial locations $l_0 = 3000\ \mu$m, $4500\ \mu$m and $5350\ \mu$m, are shown in Fig. 2a, 2b and 2c, respectively. For each case with the different initial position l_0, the snapshots were displayed at different dimensionless time $t^* = t/t_t$, where t_t is the total evaporation lifetime of each case. The corresponding evolutions of contact angles of the droplets during evaporation are presented in Fig. 2d. Similar to our findings of droplet evaporation between two parallel hydrophobic surfaces [35], the apparently prolonged evaporation time (2 hours) of the droplets dwelling between non-parallel surfaces indicates that evaporation was also greatly suppressed therein due to the substantial vapor enrichment within the confined space. However, the continuously shrinking contact line and the contact angle distribution of the evaporating droplet in the configuration of non-parallel surfaces are not symmetric anymore. And all the three confined droplets were observed to spontaneously transport towards the cusp O during evaporation. To quantitatively study the transport process, the corresponding contact line motions, lateral displacements and velocities of the evaporating droplets are illustrated in Fig. 3a-c, respectively.

As shown in Fig. 3a, even at the early stage of droplet evaporation ($t \leq 1500\ s$), the receding motions of the contact line were distinctly asymmetric: (a) For the case with $l_0 = 5350\ \mu$m, both the left and right sides of the contact line moved towards the cusp; (b) For the case with $l_0 = 4500\ \mu$m, only the right side contact line moved towards the cusp while the left side contact line got pinned; (c) For the case of $l_0 = 3000\ \mu m$, the right side contact line got pinned while the left side contact line receded away from the cusp. Correspondingly, during this early stage, the initial moving directions of the droplets were totally different for these three cases with different initial states, *i.e.*, the confined droplet with the farthest initial location from the cusp O ($l_0 = 5350\ \mu m$) would move towards the cusp while the droplet with the nearest initial location from the cusp O ($l_0 = 3000\ \mu m$) would move away from the cusp, which are manifested by the increasing or decreasing l shown in Fig. 3b and the different signs of velocity shown in Fig. 3c. Moreover, the opposite directions of droplet movement in this stage are consistent with the distinct contact angle distributions ($\theta_1 < \theta_2$ with $l_0 = 3000\ \mu m$; $\theta_1 \approx \theta_2$ with $l_0 = 4500\ \mu m$; and $\theta_1 > \theta_2$ with $l_0 = 5350\ \mu m$ as shown in Fig. 2d) due to the asymmetric confinement and the existence of CAH. And if the advancing and receding contact lines are identified based on these contact angle distributions, the receding contact line is found to be always actuated earlier ($l_0 = 3000\ \mu m,\ 4500\ \mu m$) or faster ($l_0 = 5350\ \mu m$) than the advancing contact line, which can be explained by the fact that the droplet's initial contact angle at the to-be-receded side is much closer to the receding contact angle ($\theta_r \approx \theta_1 < \theta_2 < \theta_a$ for $l_0 = 3000\ \mu m$ and $\theta_r \approx \theta_2 < \theta_1 < \theta_a$ for $l_0 = 5350\ \mu m$). In essence, the evaporation-triggered lateral motion of droplets during this early stage is mainly induced by the asymmetric motion of contact lines.

After the droplets evaporated to a certain volume, all the three confined droplets began moving towards the cusp. Especially in the case of $l_0 = 3000\ \mu m$, the direction of droplet motion was reversed at $t = 1500$ s, which is in agreement with the advancing-receding transition of the contact line shown in Fig. 2d (the crossover of the $\theta_1 - t$ and $\theta_2 - t$ curves). And the directional transport of droplets towards the cusp was sustained during the majority period of their evaporation. Generally, there are two modes of locomotion during this directional transport of droplets as shown in movies S1-S7. One is the creeping mode, during which the evaporating droplet moves towards the cusp with a relatively small velocity (~0.3 μm/s) and could be regarded as a quasi-steady motion. The other is the slipping mode, during which the evaporating droplet slips a relatively long distance in a short period, *i.e.*, with a relatively faster speed. For instance, the evaporating droplet in the case of $l_0 = 5350\ \mu$m experienced a relatively large displacement during the short period of 3173 s $\sim$ 4760 s, which is confirmed by the significantly reduced l ($\Delta l = 1940\ \mu$m) as shown in Fig. 3b and the acceleration-deceleration pulse ($|v_{max}| = 2.1\ \mu$m/s) as shown in Fig. 3c. And this relatively rapid slipping motion was also observed in the cases of $l_0 = 3000\ \mu m$ and $l_0 = 4500\ \mu m$. Nevertheless, their displacement Δl in this slipping mode and the magnitude of the maximum velocity $|v_{max}|$ also decrease with decreasing l_0.

Before its complete evaporation ($t^* \geq 0.99$), the remaining droplet bridge usually got stuck near the cusp with the continuously decreasing contact angle and shrinking contact radii. Finally, upon the rupture of the evaporating liquid bridge, two sessile daughter droplets with almost identical volumes formed on the upper and lower surfaces, respectively, till their complete evaporation thereon. During the whole process, the evaporation rate of the directionally transported droplet would be significantly suppressed by the decreasing droplet height h, leading to enhanced vapor concentration in the narrower space (cusp). Besides, the contact angle evolution during evaporation and transport is mainly

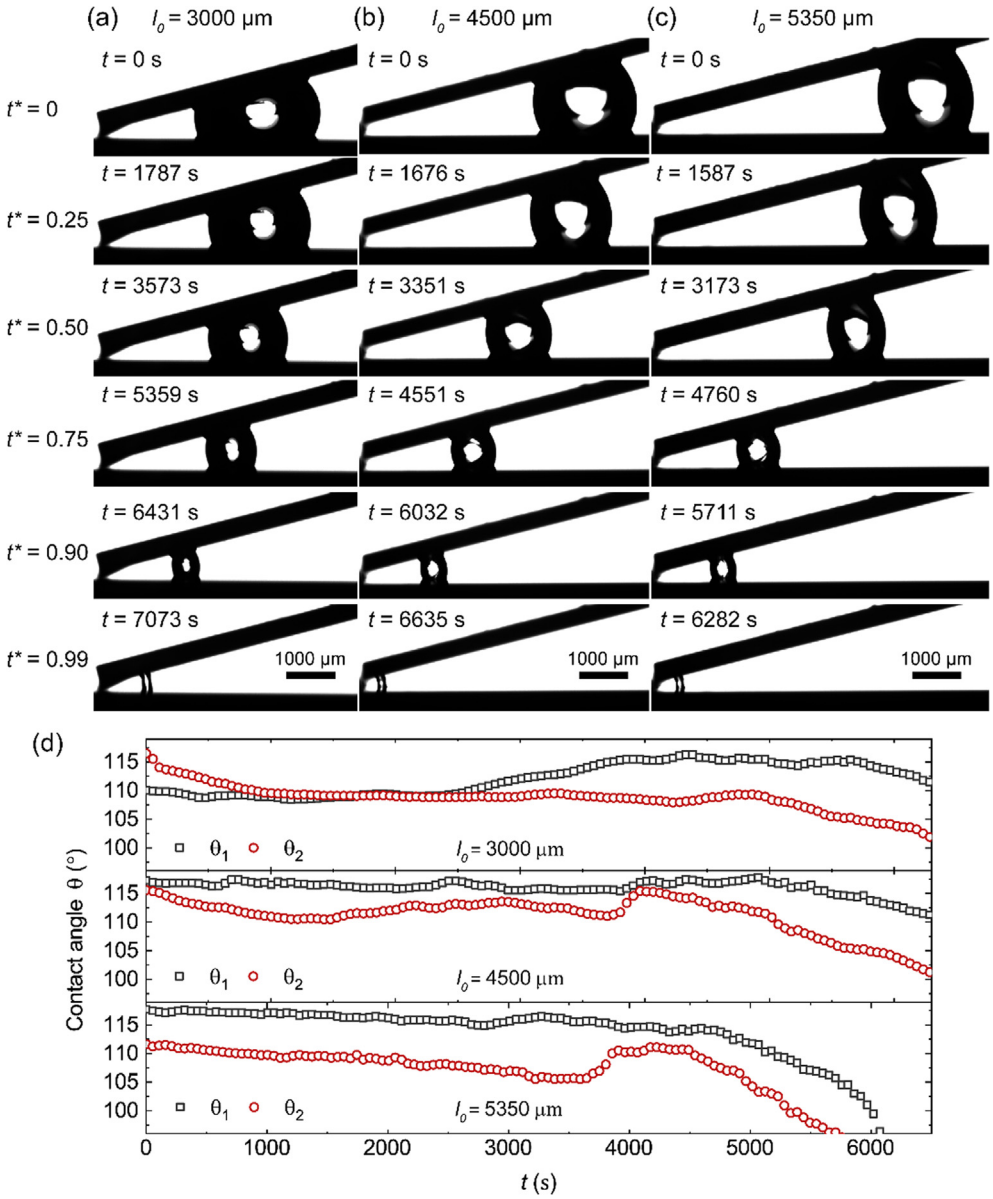

Fig. 2. Snapshots of the lateral transport of evaporating droplets with initial volume $V_0 = 4$ μL confined between two non-parallel hydrophobic surfaces with a fixed dihedral angle $\alpha = 14^\circ$ and from different initial locations (a) $l_0 = 3000$ μm, (b) $l_0 = 4500$ μm, and (c) $l_0 = 5350$ μm. (d) The corresponding evolutions of the contact angles θ_1 and θ_2 of water droplets during the evaporation and transport processes.

determined by three factors, *i.e.*, static contact angle hysteresis [42], dynamic contact angle hysteresis [42,43] and evaporation-induced contact angle reduction. As such, we found that the static contact angle hysteresis and evaporation-induced contact angle reduction are dominant in the creeping mode whereas the dynamic contact angle hysteresis is more influential in the slipping mode. Detailed discussion about droplet evaporation dynamics could be found in Section S2 and Section S4 of Supplementary Materials.

For each case with l_0 ranging from 3000 μm to 5350 μm, the droplet initially experienced stronger confinement as evidenced by their correspondingly larger deformation. Here, we define a dimensionless factor $\varphi = h/V^{1/3}$, where h is the distance between the centroids of droplet contact areas on the top and bottom plates, to quantify the magnitude of confinement on the droplet. Accordingly, the confined droplet during evaporation might be under three stress states, *i.e.*, the squeezed state (smaller φ), the stretched state (larger φ) and the moderately stressed state between those two states. We plotted the real-time variations of the confinement factor φ during droplet evaporation in Fig. 3d. The continuously increasing φ in the creeping mode indicates that the stress state of the confined droplet is gradually transferred to the stretched state. Subsequently, the occurrence of slipping motion after the apex of these $\varphi - t$ curves and the stepwise reduction of φ during the slipping mode suggest that the slipping motion might result from the stretch-induced instability with apparent deviation from the equilibrium state, which will be discussed in detail in the following section.

4.2. Energy analysis and global force analysis on the evaporating droplet

The morphologies of a 4 μL water droplet confined between two non-parallel hydrophobic surfaces with $\alpha = 14^\circ$ and at positions $l_0 = 3000$ μm, 4500 μm, and 5350 μm, respectively, were simulated by Surface Evolver. As plotted in Fig. 4a, the simulated

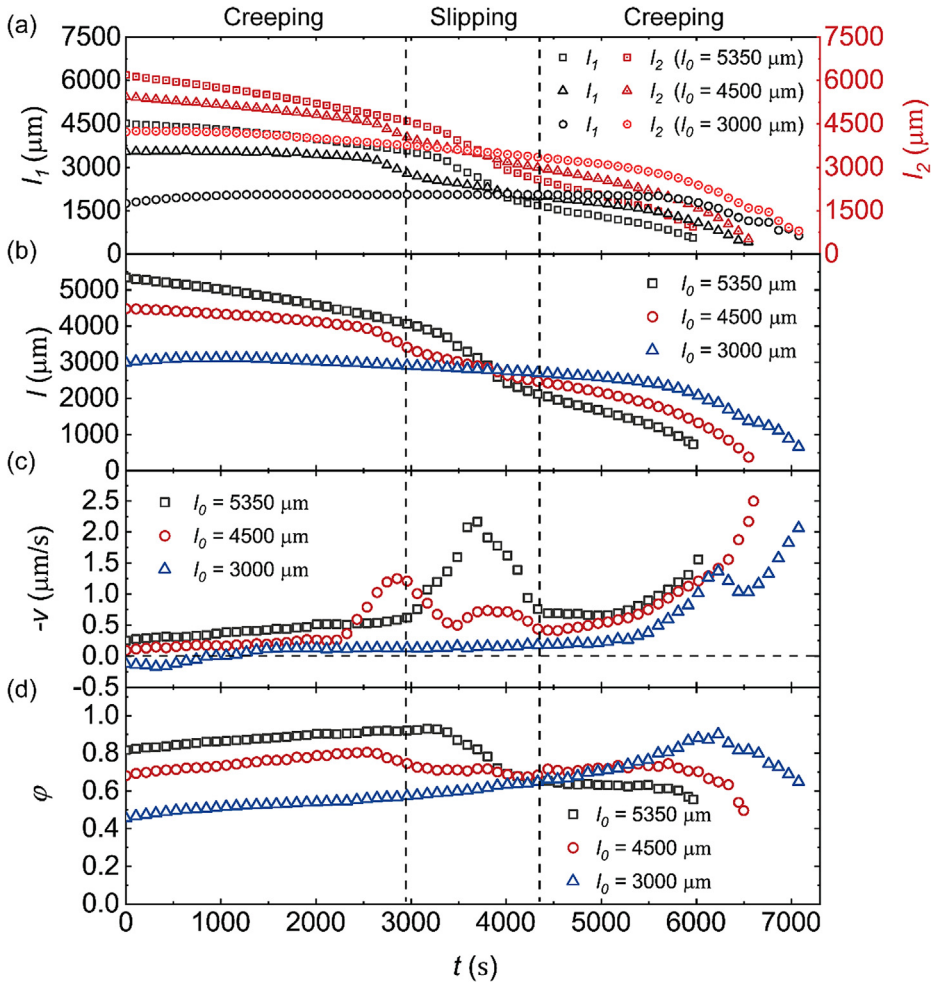

Fig. 3. (a) The displacements of the left rim l_1 and the right rim l_2 of the contact line of the confined water droplets with different initial positions l_0 during evaporation. The initial droplet volume is 4 μL. (b) The evolution of the lateral locomotion l of the confined droplets during evaporation. (c) The instantaneous velocity of the confined droplets during evaporation (the negative sign of $-v$ denotes the motion is in the opposite direction of $+x$ as shown in Fig. 1a, *i.e.*, towards the apex). (d) The evolution of the confinement factor φ of the evaporating droplets with different initial positions. The creeping-slipping-creeping modes marked on top correspond to the case of $l_0 = 5350$ μm.

morphologies of the confined droplets for these cases are consistent with the experimental snapshots at $t = 0$ *s* as shown in Fig. 2-a-c. According to our simulation, different geometric confinements and constraints on the droplet at different locations do result in different contact angle distributions as shown in Fig. 4(b), indicating that the contact angle θ would evolve from θ_1 at the leftmost rim to θ_2 at the rightmost rim along the periphery of the contact area. As droplet location changes from $l_0 = 5350$ μm to $l_0 = 3000$ μm, the evolution of contact angle distribution in the x-y plane (Fig. 1c) is consistent with the experimentally measured initial contact angle θ_1 and θ_2 as shown in Fig. 2d, which validates our simulation results. Moreover, the distributions of the friction force F_f' along the contact line are distinct as displayed in Fig. 4 (c), which are in excellent agreement with the different directions of droplet actuation at the onset of evaporation as discussed in the previous section.

To investigate the effects of the lateral position and hence the local asymmetric constraint on droplet dynamics, we fixed the dihedral angle $\alpha = 14^\circ$ and simulated the morphology evolution of a confined droplet with its volume V in the range of $0 - 4$ μL at different locations of $l \sim 2300$ μm $- 6500$ μm. Based on Eq. (13), an equilibrium position l_e with the minimum free energy G could be located for a droplet with a certain volume, which is manifested by the valley of each $G - l$ curve in Fig. 5a. Being that the contact angle hysteresis was taken in to account in our simulation, the equilibrium position is actually located within a zone, which is demarcated by the minimum boundary l_{emin} and the maximum boundary l_{emax}, rather than a specific location. Essentially, the droplet is self-propelled towards this equilibrium zone to minimize its free energy G. Therefore, the observed opposite directions of droplet actuations in the cases of $l_0 = 3000$ μm and 5350 μm at the beginning of evaporation could be elucidated as the relocation process of the confined droplet towards its instantaneous equilibrium zone. For a droplet with a certain volume, the relocation of the droplet would eventually end with its settlement in the equilibrium zone ($l_{emin} \leq l_e \leq l_{emax}$). However, in the case of an evaporating droplet with decreasing volume V, the equilibrium location $l_e \sim \alpha^{-1}V^{1/3}$ of the droplet is found to shift towards the cusp O with the continuously shrinking volume (Fig. 5a), finally reaching the cusp with its complete evaporation, *i.e.*, $l_e = 0$ with $V = 0$. As shown in movie S8, the evaporation-induced decreasing l_e should be the origin of the directional transport of an evaporating droplet towards the cusp of the non-parallel surfaces.

Based on Eqs. (5)–(9), the Laplace-pressure-induced force F_p', the friction force F_f' and the normal adhesion force F_n' exerted on

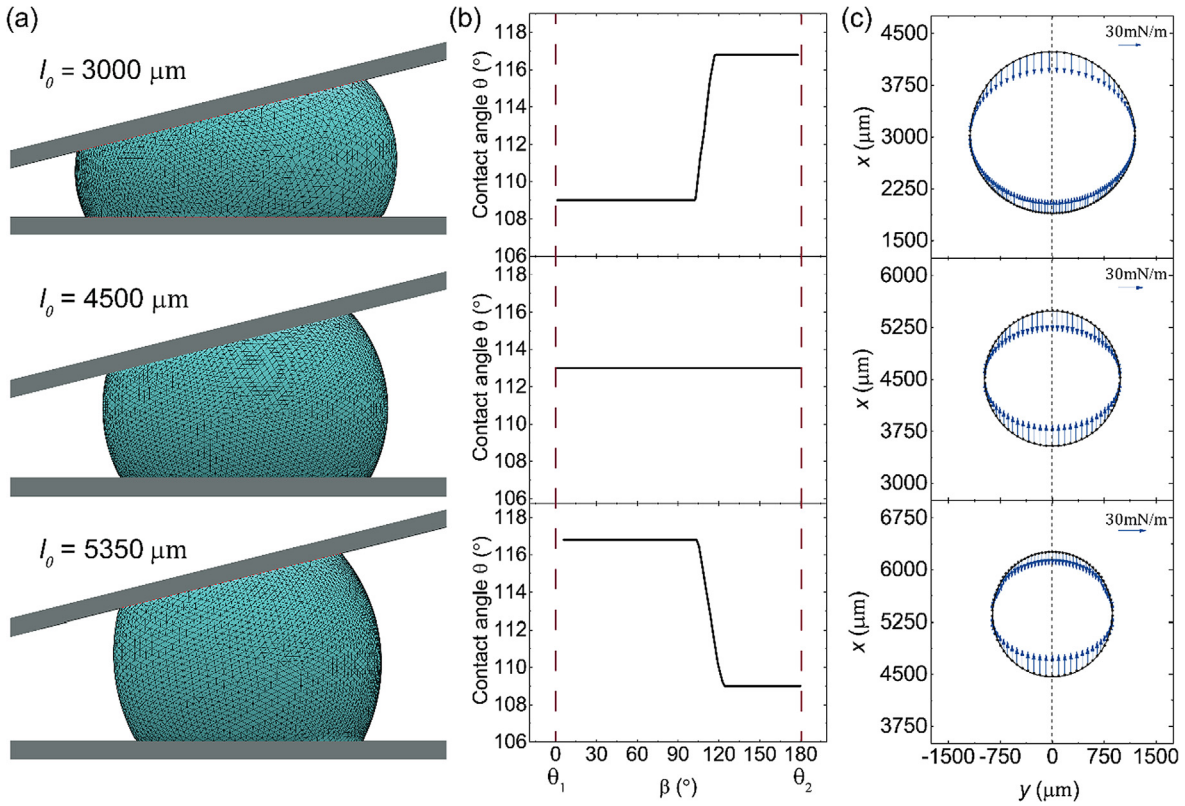

Fig. 4. For water droplets confined between two non-parallel hydrophobic surfaces with $\alpha = 14^\circ$: (a) The simulated equilibrium shapes of a 4 μL water droplet confined at various locations; (b) The contact angle θ distribution along the contact zone obtained by Surface Evolver. (c) The corresponding friction force F_f distribution along the contact zone obtained by Surface Evolver. The dashed line is the bisector. The advancing contact angle θ_a and the receding contact angle θ_r in this simulation were set at 117° and 109°, respectively.

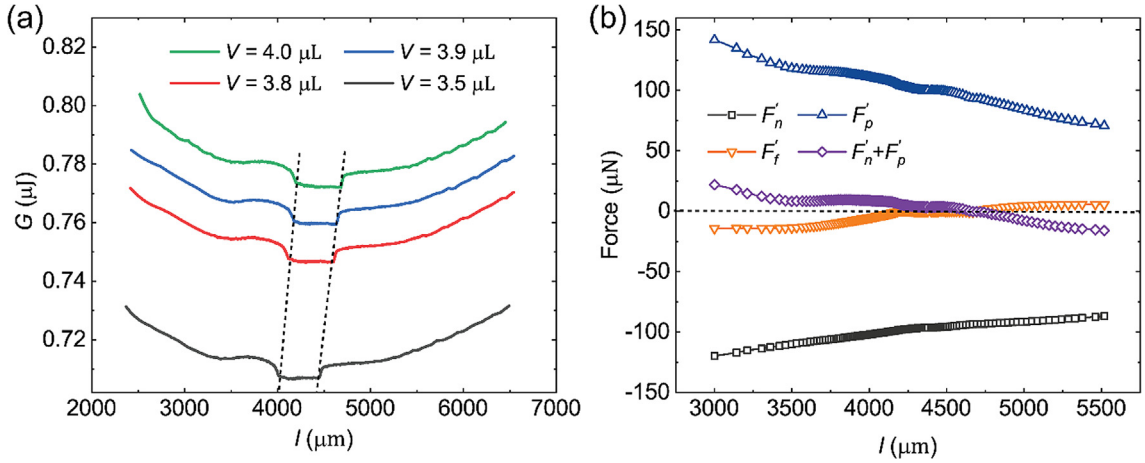

Fig. 5. (a) The evolution of the free energy G of the confined droplet of 4 μL with the varying lateral location l as the volume of the evaporating droplet decreases. The valley of G shifts towards the left (cusp) with the shrinking droplet volume. (b) The evolution of the force components on a confined droplet of 4 μL at different lateral positions. In this simulation, the non-parallel plates have the dihedral angle $\alpha = 14^\circ$.

a 4 μL confined droplet were calculated and plotted versus the corresponding droplet position l in Fig. 5b. The equilibrium zone (4250 μm $\leq l_e \leq$ 4670 μm) based on our energy analysis is consistent with the mechanical equilibrium location where the normal adhesion force $\boldsymbol{F}_n'$ is balanced with the Laplace-pressure-induced force $\boldsymbol{F}_p'$ (the friction force $\boldsymbol{F}_f'$ would become negligible in this force-balanced zone due to the small contact angle difference $|\theta_1 - \theta_2|$). This consistency could be validated by the re-derivation of the scaling law of equilibrium position $l_e \sim \alpha^{-1}V^{1/3}$ in Eq. (13) by assuming $|\boldsymbol{F}_n'| = |\boldsymbol{F}_p'|$ based on Eqs. (5)–(9):

$$\frac{2\sin\theta - 1}{\cos\theta} = \frac{2r}{h} \tag{14}$$

Also based on the two approximations that the droplet volume could be estimated as $V \approx \pi r^2 h$ and the droplet height could be approximated as $h \approx \alpha l$, then the equilibrium position l_e could be derived as:

$$l_e = k_f\left(\frac{16V}{\pi\alpha^3}\left(\frac{\cos\theta}{2\sin\theta - 1}\right)^2\right)^{\frac{1}{3}} \sim \alpha^{-1}V^{\frac{1}{3}} \quad (15)$$

where k_f is a correcting factor to the assumptions that we have made. Based on our simulation results of Surface Evolver, Eq. (15) could successfully predict l_e if the correction factor k_e in Eq. (13) and k_f in Eq. (15) are taken as 1.19 and 0.66, respectively.

Therefore, from the perspective of force balance, the relocation of an evaporating droplet towards a position with the minimum free energy G could also be interpreted as the competing result between F_n' and F_p'. As such, if $l < l_{emin}$, F_p' is the force driving the droplet away from the cusp; if $l > l_{emax}$, F_n' is the force propelling the droplet towards the cusp; and if $l_{emin} \leqslant l \leqslant l_{emax}$, the droplet remains static due to the force balance.

The effects of surface wettability on the directional transport of evaporating droplets could also be predicted based on our force analysis. For a droplet confined between two hydrophobic surfaces, as the contact angle θ decreases during evaporation, the normal adhesion force F_n' would gradually increase and approach the maximum value at $\theta = 90°$ whereas the Laplace pressure-induced force F_p' would decrease towards the minimum value due to the decreasing surface curvature H. Therefore, the smaller F_p' and the larger F_n' should be two of the main sources of the acceleration near the end of evaporation as shown in Fig. 3c. In particular, the smaller resultant force of $F_n' + F_p'$ on the stronger hydrophobic surfaces or the superhydrophobic surfaces (with $\theta > 150°$) could explain the failure of directional transport of evaporating droplets confined between two micro-structured superhydrophobic surfaces as shown in Section S5 of Supplementary Materials.

The simulated equilibrium zone of an evaporating droplet with the diminishing volume V from 4 μL to 0 μL were fitted and plotted in Fig. 6a, in which the whole map is divided by the curves of l_{emax} and l_{emin} into three regimes for the confined droplet, *i.e.*, the squeezed (SQ) regime ($F_n' > F_p'$ while $l < l_{emin}$), the equilibrium (EQ) regime ($F_n' \approx F_p'$ while $l_{emin} \leqslant l \leqslant l_{emax}$), and the stretched (ST) regime ($F_n' < F_p'$ while $l > l_{emax}$). In this phase map, we also plotted the experimentally measured displacements of three evaporating droplets confined between two non-parallel hydrophobic plates from different initial positions $l_0 = 3000$ μm, 4500 μm, and 5350 μm, respectively. It can be seen that the three droplets were initially located in three different regimes at the onset of their evaporation. And the characteristics of this evaporation-triggered transport could be summarized from the map. Despite its initial state, the evaporating droplet would follow the complete or partial sequence of SQ → EQ → ST → EQ in a successive fashion. For example, the droplet at the initially squeezed regime ($l_0 = 3000$ μm) followed the complete sequence of SQ → EQ → ST → EQ. Whereas the droplet initially at the stretched regime ($l_0 = 5350$ μm) only experienced the last step of the transition, *i.e.*, from the stretched regime to the equilibrium regime (ST → EQ).

To further clarify the origin of this evaporation-triggered motion and the two distinct modes during the transport, we defined the dimensionless deviation factor $e = (l - \bar{l}_e)/V^{1/3}$ where $\bar{l}_e = (l_{emin} + l_{emax})/2$. And the instantaneous evolutions of deviation factor e for the three cases are depicted in Fig. 6b. Indeed, the value and the sign of the deviation factor e could be used to quantify the direction and the relative magnitude of the acceleration of the evaporating droplet, respectively, *i.e.*, the droplet at the location with a larger deviation always owns the stronger acceleration pointing towards the equilibrium zone ($e = 0$). As shown in Fig. 6b, the deviation factor e started increasing from the beginning of evaporation, indicative of the procrastinated droplet motion in the creeping mode while accumulating deviation. Once the droplet reached a certain location with the largest deviation, the stimulated instability finally drove the droplet to slip towards the equilibrium state in a very short period (*i.e.*, slipping mode). The similar spontaneous motion of a liquid bridge between two non-parallel hydrophilic surfaces due to the instability had been reported in several previous studies [25,31,44]. During the whole transport process, each evaporating droplet kept oscillating around its instantaneous equilibrium location ($e = 0$), indicating that the dynamics of an evaporating droplet could be regarded as a self-relaxation process from the squeezed state or the stretched state to the equilibrium state. Therefore, it is reasonable to arrange the droplet initially at the stretched state with a larger e to take advantage of this unstable slipping motion for quicker transport of the evaporating droplet.

4.3. The effects of dihedral angle on the lateral transport of evaporating droplets

To investigate the effects of geometric confinement on droplet evaporation and transport dynamics between two non-parallel

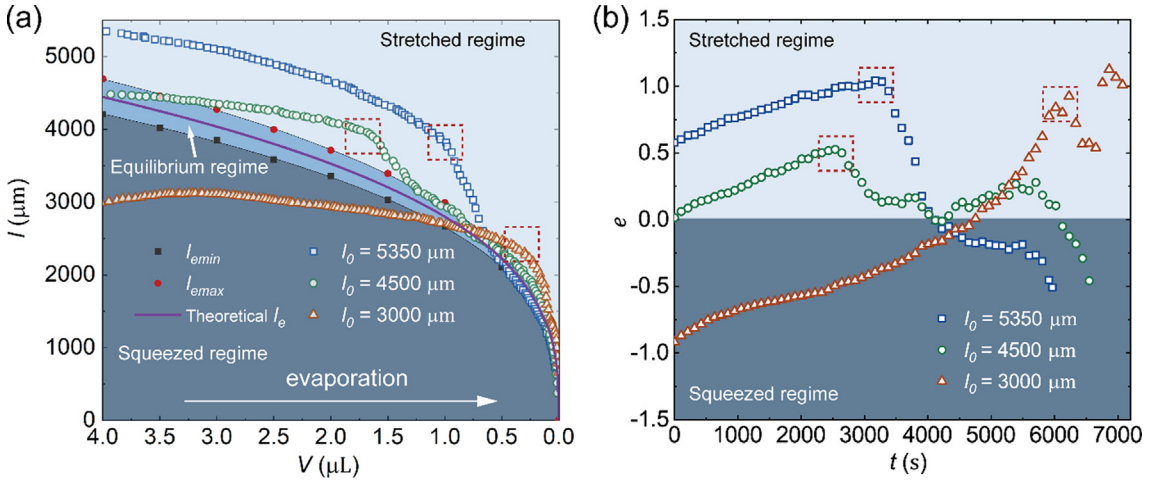

Fig. 6. For water droplets of 4 μL confined between two non-parallel hydrophobic surfaces with $\alpha = 14°$: (a) Starting from different initial location l_0, the lateral displacement l of the evaporating droplets with shrinking volume V; and the relaxation map of the confined droplets at different location l with varying volume V. (b) The evolution of dimensionless deviation e of the evaporating droplets from the instantaneous equilibrium location l_e during the transport. The red dashed square on each curve indicates the creeping-slipping mode transition. (For interpretation of the references to colour in this figure legend, the reader is referred to the web version of this article.)

hydrophobic surfaces, the dihedral angles α of the two surfaces was varied from 10° to 22° while the initial location l_0 of droplets were tuned to ensure the droplets in the similar stretched regime, *i.e.*, setting the initial height of each confined droplet $h_0 \approx h_s$, where h_s is the initial height of the sessile droplet deposited on the bottom surface. Fig. 7a-c are the representative snapshots of the directional transport of evaporating droplets confined between two non-parallel hydrophobic surfaces with $\alpha = 10^\circ$, 18°, and 22°, respectively. As expected, all the confined droplets were eventually transported towards the cusp of the two non-parallel surfaces. With the increasing dihedral angle α, the droplet would reach closer to the cusp at the end of its complete evaporation, which is evidenced by the fact that the droplet in the configuration of dihedral angle $\alpha = 10^\circ$ finally detached from the upper surface at $l = 1700$ μm whereas the droplet finally reached the cusp O in the case of $\alpha = 22^\circ$.

The displacements and instantaneous velocities of the evaporating droplets for cases of $\alpha = 10^\circ, 14^\circ, 18^\circ$, and 22° are illustrated in Fig. 7d-e, respectively. Both the creeping mode and the slipping mode of droplet motion were observed in the cases of $\alpha = 10^\circ$, 14°, and 18°, whereas the droplet was observed to move only in the creeping mode between surfaces with $\alpha = 22^\circ$. Moreover, the crest of droplet velocity in the acceleration-deceleration process of the slipping mode decreases as α increases. To elucidate the depressed slipping mode with increasing dihedral angle α, we further numerically obtained the equilibrium locations l_{emin}, l_{emax} and l_e of the confined droplets with volume V in the range of 0 – 10 μL between two non-parallel hydrophobic surfaces with dihedral angle α in the range of 10° – 22°. The linear relationship between l_e and $\alpha^{-1}V^{1/3}$ as shown in Fig. 8a validates our scaling law of $l_e \sim \alpha^{-1}V^{1/3}$ (Eqs. (13) and (15)). Besides, the values of l_{emin} and l_{emax} can be regressed in the form of $l_e = CV^{1/3}$ (C is a constant

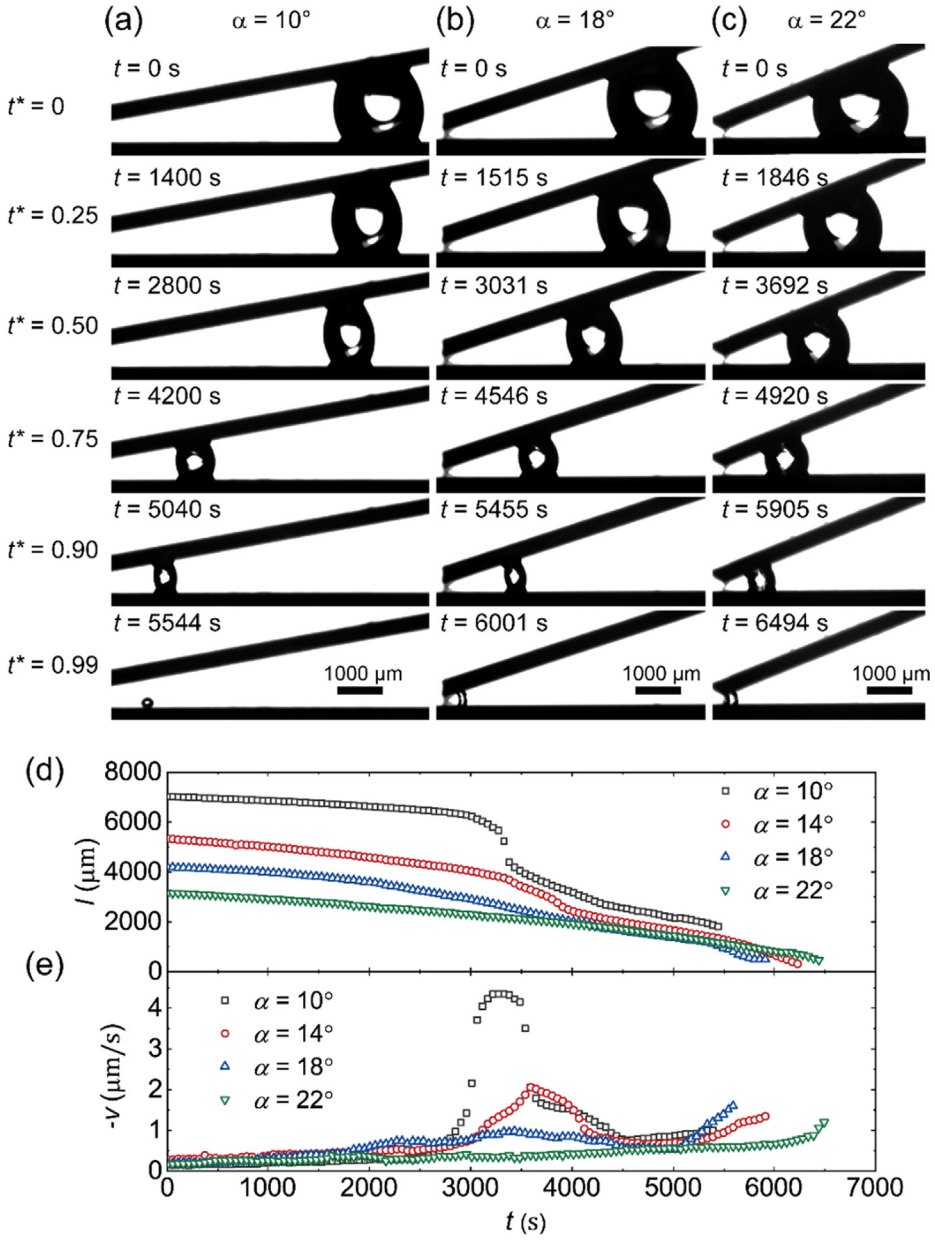

Fig. 7. The snapshots of the lateral transport of evaporating droplets of 4 μL confined between two non-parallel hydrophobic surfaces with dihedral angle (a) $\alpha = 10^\circ$, (b) $\alpha = 18^\circ$, (c) $\alpha = 22^\circ$, respectively. (d) The corresponding lateral transport of the evaporating droplets and (e) The evolution of the velocity of the transporting droplets between two non-parallel hydrophobic surfaces with α in the range of 10° – 22°.

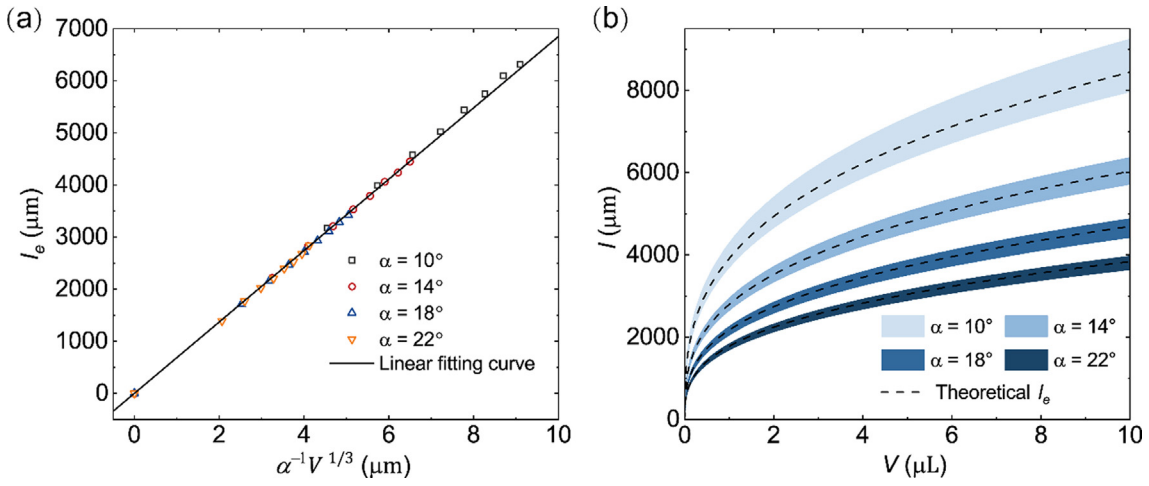

Fig. 8. (a) The simulated equilibrium position l_e of the confined droplet follows a linear relationship of $l_e \sim \alpha^{-1}V^{1/3}$ during evaporation. (b) The phase map of the relaxation states of the confined droplets with different droplet locations and volumes in the non-parallel hydrophobic surfaces with varying dihedral angle α. The bandwidth of each equilibrium zone is demarcated by l_{emin} and l_{emax}, respectively.

coefficient varying for l_{emin} and l_{emax}), demarcating the bandwidth of each equilibrium zone as plotted in Fig. 8b.

As shown in Fig. 8b, for an evaporating droplet confined between two non-parallel hydrophobic surfaces with dihedral angle α, the overall trend of the $l_e - V$ evolution becomes more flattened with increasing α, indicating that the equilibrium location l_e would laterally shift a shorter distance for the same volume reduction in the configuration with a larger α. For instance, if droplet volume is reduced from 10 μL to 6 μL, the corresponding equilibrium position shifts $\Delta l_e \approx 1500$ μm for the case of $\alpha = 10^\circ$ whereas $\Delta l_e \approx 600$ μm for the case of $\alpha = 22^\circ$. Nonetheless, regarding the four cases with varying α in the range of 10°–22°, the displacements of droplets in the creeping mode before the slipping motion are very small and almost identical. Therefore, for the case with the smallest dihedral angle $\alpha = 10^\circ$, the deviation e from the droplet real-time location l to the equilibrium location l_e became so large ($e_{max} \sim 2.45$) that the instability could trigger the droplet to slip over a relatively longer distance to the equilibrium location l_e. For the case with the largest dihedral angle $\alpha = 22^\circ$, the deviation e was relatively small ($e_{max} \sim 0.39$) during the whole process so that no apparent slipping motion could be observed in this case. Furthermore, as the dihedral angle α increases, the bandwidth of the equilibrium zone gradually decreases, indicating that the influence of CAH on droplet motion becomes weaker due to the stronger component of the driving force associated with a larger dihedral angle α (Eq. (9)).

Note that the phase map of Fig. 8b can be used to not only elucidate the transport mechanism of an evaporating droplet but also to predict the dynamics of a droplet confined between two non-parallel surfaces under the open/close [34] or squeezed/stretched [23] cycles. Moreover, this map could be applied to explain the suspension of growing embryos inside the V-shaped cavity in the micro-structured surface during dropwise condensation [34,45,46]. If the condensate embryo is initially formed at the bottom of the surface cavity, the growing embryo/droplet will continuously move upward since the instantaneous equilibrium position l_e keeps moving away from the cavity base in the order of $\alpha^{-1}V^{1/3}$ (Eqs. (13) and (15)).

5. Conclusion

In this study, the directional transport of an evaporating droplet confined between two non-parallel hydrophobic surfaces is theoretically, experimentally, and numerically investigated. Even though the asymmetric contact line motions of either shrinking or growing droplets inside V-shaped grooves have been reported in only few previous studies [27,34], however, in their analyses, the asymmetric motions were simply attributed to capillary forces [34] and the driving effect of gravity on droplets could not be excluded in their vertical configurations [27,34]. In contrast, the evaporation-triggered droplet transport observed by us is indicative of an intriguing actuation mechanism, which is generally ignored in state-of-the-art modeling of droplets in complex structures [23,27,34,39,47,48] or microfluidics in a porous medium [49,50]. Therefore, a systematic investigation and deeper understanding of the droplet dynamics under asymmetric confinement is still entailed.

According to our Surface Evolver simulation and theoretical analysis, an equilibrium location l_e of a confined droplet owning the lowest surface energy G and force balance is recognized. Intriguingly, along with the evaporation-induced volume reduction, evaporating droplet would chase this instantaneous equilibrium location l_e, which consecutively shifts towards the cusp of the two non-parallel surfaces (Movie S8). Here, the scaling law of the morphology/volume-dependent equilibrium location is theoretically unveiled, which could not only elucidate the directional transport of the shrinking droplet during evaporation [27,34] or the growing embryo during condensation [34,45,46] inside the asymmetric geometric structures, but also explain the motion dynamics of droplets being asymmetrically squeezed or stretched as reported in several prior studies [22,23,34]. Moreover, two kinds of droplet motion modes, *i.e.*, the creeping mode and the slipping mode, were observed during the evaporation-incurred transport process. Here, the creeping motion of an evaporating droplet could be regarded as a self-relaxation process to dispose of the confinement. The slipping mode of motion occurring at the stretched regime is ascribed to the accumulated instability, which is manifested by the relatively larger deviation e from the equilibrium location.

In contrast to the majority of studies that treated droplet evaporation [35,51] and transport [52–54] as two independent procedures, this study is the first work considering these two processes in a combined manner, which provides us a new avenue to achieve solvent transport and analyte/colloidal particle concentration in parallel. As such, on the droplet-based microfluidic platform [2,3], both the deposition location and morphology of the self-assembled micro/nanoparticles can be more accurately

predicted and controlled in a passive and decisive approach, which deserves further exploration in the future.

Declaration of Competing Interest

The authors declare that they have no known competing financial interests or personal relationships that could have appeared to influence the work reported in this paper.

Acknowledgement

This work is financially supported by NSF CBET under grant number 1550299 and NSF ECCS under grant number 1808931.

Appendix A. Supplementary material

Supplementary data to this article can be found online at https://doi.org/10.1016/j.jcis.2021.06.164.

References

[1] M. Zhang, W. Cheng, Z. Zheng, J. Cheng, J. Liu, Meridian whispering gallery modes sensing in a sessile microdroplet on micro/nanostructured superhydrophobic chip surfaces, Microfluid. Nanofluid. 23 (9) (2019) 106.
[2] L.R. Shang, Y. Cheng, Y.J. Zhao, Emerging Droplet Microfluidics, Chem. Rev. 117 (12) (2017) 7964–8040.
[3] S.Y. Teh, R. Lin, L.H. Hung, A.P. Lee, Droplet microfluidics, Lab Chip 8 (2) (2008) 198–220.
[4] M. Grzelczak, J. Vermant, E.M. Furst, L.M. Liz-Marzán, Directed self-assembly of nanoparticles, ACS Nano 4 (7) (2010) 3591–3605.
[5] K. Thorkelsson, P. Bai, T. Xu, Self-assembly and applications of anisotropic nanomaterials: A review, Nano Today 10 (1) (2015) 48–66.
[6] L. Hu, M. Chen, X. Fang, L. Wu, Oil-water interfacial self-assembly: a novel strategy for nanofilm and nanodevice fabrication, Chem. Soc. Rev. 41 (3) (2012) 1350–1362.
[7] M.A. Boles, M. Engel, D.V. Talapin, Self-Assembly of Colloidal Nanocrystals: From Intricate Structures to Functional Materials, Chem. Rev. 116 (18) (2016) 11220–11289.
[8] J. Song, W. Cheng, M. Nie, X. He, W. Nam, J. Cheng, W. Zhou, Partial Leidenfrost Evaporation-Assisted Ultrasensitive Surface-Enhanced Raman Spectroscopy in a Janus Water Droplet on Hierarchical Plasmonic Micro-/Nanostructures, ACS Nano 14 (8) (2020) 9521–9531.
[9] G. Cristobal, L. Arbouet, F. Sarrazin, D. Talaga, J.L. Bruneel, M. Joanicot, L. Servant, On-line laser Raman spectroscopic probing of droplets engineered in microfluidic devices, Lab Chip 6 (9) (2006) 1140–1146.
[10] S.K. Kuster, S.R. Fagerer, P.E. Verboket, K. Eyer, K. Jefimovs, R. Zenobi, P.S. Dittrich, Interfacing Droplet Microfluidics with Matrix-Assisted Laser Desorption/Ionization Mass Spectrometry: Label-Free Content Analysis of Single Droplets, Anal. Chem. 85 (3) (2013) 1285–1289.
[11] Y.M. Zheng, H. Bai, Z.B. Huang, X.L. Tian, F.Q. Nie, Y. Zhao, J. Zhai, L. Jiang, Directional water collection on wetted spider silk, Nature 463 (7281) (2010) 640–643.
[12] J. Ju, H. Bai, Y.M. Zheng, T.Y. Zhao, R.C. Fang, L. Jiang, A multi-structural and multi-functional integrated fog collection system in cactus, Nat. Commun. 3 (1) (2012) 1–6.
[13] H.G. Andrews, E.A. Eccles, W.C.E. Schofield, J.P.S. Badyal, Three-Dimensional Hierarchical Structures for Fog Harvesting, Langmuir 27 (7) (2011) 3798–3802.
[14] K.H. Chu, R. Xiao, E.N. Wang, Uni-directional liquid spreading on asymmetric nanostructured surfaces, Nat. Mater. 9 (5) (2010) 413–417.
[15] M.K. Chaudhury, G.M. Whitesides, How to Make Water Run Uphill, Science 256 (5063) (1992) 1539–1541.
[16] R.H. Farahi, A. Passian, T.L. Ferrell, T. Thundat, Microfluidic manipulation via Marangoni forces, Appl. Phys. Lett. 85 (18) (2004) 4237–4239.
[17] W. Cheng, J. Liu, Z. Zheng, X. He, B. Zheng, H. Zhang, H. Cui, X. Zheng, T. Zheng, B.E. Gnade, J. Cheng, Adaptive optical beam steering and tuning system based on electrowetting driven fluidic rotor, Commun. Phys. 3 (1) (2020) 1–9.
[18] J.T. Cheng, C.L. Chen, Active thermal management of on-chip hot spots using EWOD-driven droplet microfluidics, Exp. Fluids 49 (6) (2010) 1349–1357.
[19] H. Mertaniemi, V. Jokinen, L. Sainiemi, S. Franssila, A. Marmur, O. Ikkala, R.H.A. Ras, Superhydrophobic Tracks for Low-Friction, Guided Transport of Water Droplets, Adv. Mater. 23 (26) (2011) 2911–2914.
[20] C. Mandal, U. Banerjee, A.K. Sen, Transport of a Sessile Aqueous Droplet over Spikes of Oil Based Ferrofluid in the Presence of a Magnetic Field, Langmuir 35 (25) (2019) 8238–8245.
[21] Q.Q. Sun, D.H. Wang, Y.N. Li, J.H. Zhang, S.J. Ye, J.X. Cui, L.Q. Chen, Z.K. Wang, H. J. Butt, D. Vollmer, X. Deng, Surface charge printing for programmed droplet transport, Nat. Mater. 18 (9) (2019) 936–941.
[22] L.Y. Wang, H.A. Wu, F.C. Wang, Efficient transport of droplet sandwiched between saw-tooth plates, J. Colloid Interface Sci. 462 (2016) 280–287.
[23] M. Ataei, H.C. Chen, A. Amirfazli, Behavior of a Liquid Bridge between Nonparallel Hydrophobic Surfaces, Langmuir 33 (51) (2017) 14674–14683.
[24] X. Heng, C. Luo, Liquid Drop Runs Upward between Two Nonparallel Plates, Langmuir 31 (9) (2015) 2743–2748.
[25] C. Luo, X. Heng, M.M. Xiang, Behavior of a Liquid Drop between Two Nonparallel Plates, Langmuir 30 (28) (2014) 8373–8380.
[26] M. Prakash, D. Quere, J.W.M. Bush, Surface tension transport of prey by feeding shorebirds: The capillary ratchet, Science 320 (5878) (2008) 931–934.
[27] T. Han, H. Noh, H.S. Park, M.H. Kim, Effects of wettability on droplet movement in a V-shaped groove, Sci. Rep. 8 (1) (2018) 1–10.
[28] C. Luo, M. Mrinal, X. Wang, Self-propulsion of Leidenfrost Drops between Non-Parallel Structures, Sci. Rep. 7 (1) (2017) 1–12.
[29] J. Xu, J.F. Xia, S.W. Hong, Z.Q. Lin, F. Qiu, Y.L. Yang, Self-assembly of gradient concentric rings via solvent evaporation from a capillary bridge, Phys. Rev. Lett. 96 (6) (2006) 066104.
[30] M. Markos, V.S. Ajaev, G.M. Homsy, Steady flow and evaporation of a volatile liquid in a wedge, Phys. Fluids 18 (9) (2006) 092102.
[31] M. Ataei, H.C. Chen, T. Tang, A. Amirfazli, Stability of a liquid bridge between nonparallel hydrophilic surfaces, J. Colloid Interface Sci. 492 (2017) 207–217.
[32] E. Rabani, D.R. Reichman, P.L. Geissler, L.E. Brus, Drying-mediated self-assembly of nanoparticles, Nature 426 (6964) (2003) 271–274.
[33] R.D. Deegan, O. Bakajin, T.F. Dupont, G. Huber, S.R. Nagel, T.A. Witten, Capillary flow as the cause of ring stains from dried liquid drops, Nature 389 (6653) (1997) 827–829.
[34] W. Xu, Z. Lan, B.L. Peng, R.F. Wen, Y.S. Chen, X.H. Ma, Directional Movement of Droplets in Grooves: Suspended or Immersed?, Sci Rep. 6 (1) (2016) 1–11.
[35] X. He, J. Cheng, C.P. Collier, B.R. Srijanto, D.P. Briggs, Evaporation of squeezed water droplets between two parallel hydrophobic/superhydrophobic surfaces, J. Colloid Interface Sci. 576 (2020) 127–138.
[36] K.A. Brakke, The surface evolver, Exp. Math. 1 (2) (1992) 141–165.
[37] M.J. Santos, S. Velasco, J.A. White, Simulation Analysis of Contact Angles and Retention Forces of Liquid Drops on Inclined Surfaces, Langmuir 28 (32) (2012) 11828–11835.
[38] M.J. Santos, J.A. White, Theory and Simulation of Angular Hysteresis on Planar Surfaces, Langmuir 27 (24) (2011) 14868–14875.
[39] D. Baratian, A. Cavalli, D. van den Ende, F. Mugele, On the shape of a droplet in a wedge: new insight from electrowetting, Soft Matter 11 (39) (2015) 7717–7721.
[40] A. Shastry, M.J. Case, K.F. Bohringer, Directing droplets using microstructured surfaces, Langmuir 22 (14) (2006) 6161–6167.
[41] L. Xu, Z.G. Li, S.H. Yao, Directional motion of evaporating droplets on gradient surfaces, Appl. Phys. Lett. 101 (6) (2012) 064101.
[42] H.B. Eral, D.J.C.M. 't Mannetje, J.M. Oh, Contact angle hysteresis: a review of fundamentals and applications, Colloid Polym. Sci. 291(2) (2013) 247-260.
[43] T. Blake, J. Haynes, Kinetics of liquidliquid displacement, J. Colloid Interface Sci. 30 (3) (1969) 421–423.
[44] M. Ataei, T. Tang, A. Amirfazli, Motion of a liquid bridge between nonparallel surfaces, J. Colloid Interface Sci. 492 (2017) 218–228.
[45] X. Yan, Y. Qin, F. Chen, G. Zhao, S. Sett, M.J. Hoque, K.F. Rabbi, X. Zhang, Z. Wang, L. Li, F. Chen, J. Feng, N. Mijkovic, Laplace Pressure Driven Single-Droplet Jumping on Structured Surfaces, ACS Nano 14 (10) (2020) 12796–12809.
[46] A. Vandadi, L. Zhao, J. Cheng, Resistant energy analysis of self-pulling process during dropwise condensation on superhydrophobic surfaces, Nanoscale Adv. 1 (2) (2019) 1136–1147.
[47] P. Concus, R. Finn, Discontinuous behavior of liquids between parallel and tilted plates, Phys. Fluids 10 (1) (1998) 39–43.
[48] D. Baratian, E. Ruiz-Gutierrez, F. Mugele, R. Ledesma-Aguilar, Slippery when wet: mobility regimes of confined drops in electrowetting, Soft Matter 15 (35) (2019) 7063–7070.
[49] J.-T. Cheng, J. Morris, J. Tran, A. Lumsdaine, N. Giordano, D. Nolte, L. Pyrak-Nolte, Single-phase flow in a rock fracture: micro-model experiments and network flow simulation, Int. J. Rock Mech. Min. Sci 41 (4) (2004) 687–693.
[50] C. Chen, P. Joseph, S. Geoffroy, M. Prat, P. Duru, Evaporation with the formation of chains of liquid bridges, J. Fluid Mech. 837 (2018) 703–728.
[51] H.Y. Erbil, Evaporation of pure liquid sessile and spherical suspended drops: A review, Adv. Colloid Interface Sci. 170 (1) (2012) 67–86.
[52] S.J. Lin, B. Li, Y. Xu, A.A. Mehrizi, L.Q. Chen, Effective Strategies for Droplet Transport on Solid Surfaces, Adv. Mater. Interfaces (2020) 2001441.
[53] Y.F. Si, Z.C. Dong, Bioinspired Smart Liquid Directional Transport Control, Langmuir 36 (3) (2020) 667–681.
[54] H.Y. Dai, Z.C. Dong, L. Jiang, Directional liquid dynamics of interfaces with superwettability, Sci Adv 6 (37) (2020) eabb5528.